targets

MDPI

Article

Dual-Responsive Fluorescent Probe for Fluorescence Imaging of Superoxide Anion and Nitric Oxide During Macrophage Foam Cell Formation

Xinyu Chen [1], Jun Lu [2], Chenyu Wang [1], Wen Zhang [1], Hui Wang [1], Wei Zhang [1,*], Ping Li [1] and Bo Tang [1,2]

[1] College of Chemistry, Chemical Engineering and Materials Science, Key Laboratory of Molecular and Nano Probes, Ministry of Education, Institute of Biomedical Sciences, Shandong Normal University, Jinan 250014, China; chenxy_0317@163.com (X.C.); wcy20062022@163.com (C.W.); zhangwen@sdnu.edu.cn (W.Z.); 613006@sdnu.edu.cn (H.W.); lip@sdnu.edu.cn (P.L.); tangb@sdnu.edu.cn (B.T.)

[2] Laoshan Laboratory, Qingdao 266237, China; huaxuelujun@163.com

* Correspondence: zhangwei@sdnu.edu.cn

Abstract

Foam cell formation of macrophages is a core pathological event in the progression of atherosclerosis. Investigating the changes in active molecules during macrophage foaming is critical for the early warning and mechanistic research of atherosclerosis. Superoxide anion ($O_2^{\bullet-}$) and nitric oxide (NO) are two typical representatives of these active species; evaluating the fluctuations of $O_2^{\bullet-}$ and NO during macrophage foaming is vital for understanding the early diagnosis and pathological mechanisms of atherosclerosis. Herein, we report a fluorescent probe for the detection of $O_2^{\bullet-}$ and NO concentration changes based on the quenching effect of the urea bond and trifluoromethanesulfonate group on the fluorophore. MB-ROS features favorable sensitivity, selectivity and biocompatibility, enabling imaging of $O_2^{\bullet-}$ and NO fluctuations in macrophages. It was further validated in ox-LDL-stimulated foam cell models to visually track abnormal ROS/RNS changes during foam formation. This work offers a reliable chemical imaging tool to uncover redox imbalance underlying early atherosclerotic macrophage foaming.

Keywords: targeted probes; foam cell formation of macrophages; superoxide anion; nitric oxide

1. Introduction

Atherosclerosis (AS) is a pathological process of cardiovascular diseases characterized by lipid deposition in arterial walls, chronic inflammatory responses and plaque formation, which serves as a critical pathological basis for severe cardio-cerebrovascular events such as coronary heart disease and stroke [1,2]. The occurrence and progression of AS involve multiple pathological factors, including lipid metabolism disorder, inflammatory cell infiltration and vascular redox microenvironment imbalance [3]. Among these pathological events, the uptake of oxidized low-density lipoprotein (ox-LDL) by macrophages and subsequent foam cell formation represent the key event for early plaque formation and disease progression of AS [4,5]. Therefore, the development of analytical tools capable of real-time monitoring the changes in key bioactive molecules during the macrophage foaming process is of great significance for revealing the early pathological mechanism of AS and evaluating disease progression.

Academic Editor: Shile Huang

Received: 24 June 2026
Revised: 5 August 2026
Accepted: 7 August 2026
Published: 11 August 2026

Macrophage foaming is a process accompanied by continuous amplification of oxidative stress and inflammatory signals [6]. During this process, abnormal generation of reactive oxygen species (ROS) and reactive nitrogen species (RNS) will disrupt intracellular redox homeostasis and further promote lipid accumulation and inflammatory responses [7–9]. Superoxide anion ($O_2^{\bullet-}$) is a pivotal member of ROS, which participates in the regulation of inflammation-related signaling pathways such as NF-κB and plays an essential role in the amplification process of oxidative stress [10–13]. As a critical RNS, nitric oxide (NO) can regulate vascular tone, inhibit platelet aggregation and maintain vascular microenvironment homeostasis under physiological conditions [14,15]. Nevertheless, during the process of ox-LDL stimulation and macrophage foaming, the abnormal elevation of NO is closely correlated with inflammatory activation, enhanced oxidative stress and foam cell formation [7,16–18]. More importantly, $O_2^{\bullet-}$ and NO do not exist independently, and their synergistic variations directly reflect the ROS/RNS imbalance state in macrophages [19,20]. Accordingly, achieving simultaneous and real-time visualized detection of $O_2^{\bullet-}$ and NO is of great value for in-depth understanding of the redox process during macrophage foaming and tracking disease progression.

Fluorescent probes possess multiple superior properties, including high sensitivity, high spatiotemporal resolution, biocompatibility and suitability for living cell imaging, which have emerged as vital analytical tools for investigating the variations in active molecules in complex biological systems. At present, most fluorescent probes applied in macrophage foaming research focus on the detection of single active species, which are difficult to comprehensively reflect the correlated variations between ROS and RNS [21–24]. In addition, single-response signals are susceptible to non-specific interference in the complex cellular microenvironment, which may impair the accuracy and reliability of detection results. In contrast, dual-response fluorescent probes can monitor two key molecules in the same system, which not only contributes to the improvement of detection efficiency but also can provide more comprehensive pathological information [25,26]. Therefore, the detection of $O_2^{\bullet-}$ and NO alterations during macrophage foam cell formation is of critical significance for in-depth elucidation of the intracellular redox process in foam cell formation and tracking the progression of related pathological conditions.

On this basis, this work designs and synthesizes a dual-response fluorescent probe named MB-ROS, which is applied for the simultaneous detection of $O_2^{\bullet-}$ and NO during the macrophage foaming process. The probe adopts naphthalimide and methylene blue as the respective responsive fluorescent units for $O_2^{\bullet-}$ and NO, which are connected through a urea bond to realize independent fluorescent responses towards the two active species. MB-ROS exhibits sensitivity, selectivity and biocompatibility, which can be applied for the detection of the level variations in $O_2^{\bullet-}$ and NO in macrophages. Furthermore, the probe has been successfully applied in the ox-LDL-induced macrophage foaming model, realizing visualized monitoring of the abnormal variations in ROS/RNS during the foaming process. This study provides an effective chemical imaging tool for elucidating the redox imbalance process related to macrophage foaming in the early stage of AS.

2. Materials and Methods

2.1. Materials and Instruments

All reagents were of analytical grade. Common reagents and solvents were purchased from Sinopharm Chemical Reagent Co., Ltd. (Shanghai, China) Triphosgene and di-tert-butyl dicarbonate were obtained from Shanghai Aladdin Biochemical Technology Co., Ltd. (Shanghai, China) N-Boc-ethylenediamine, 4-bromo-1,8-naphthalic anhydride, N-hydroxysuccinimide, trifluoroacetic acid and methylene blue were supplied by Shanghai Macklin Biochemical Co., Ltd. (Shanghai, China) N-

phenylbis(trifluoromethanesulfonimide) was purchased from Shanghai Bide Pharmatech Co., Ltd. (Shanghai, China) 2-Methoxyestradiol was obtained from Shanghai Yuanye Bio-Technology Co., Ltd. (Shanghai, China) Carboxy-PTIO was supplied by Shanghai Beyotime Biotechnology Co., Ltd. (Shanghai, China) Cell Counting Kit-8 (CCK-8) assay reagent was purchased from MedChemExpress (Shanghai, China). Fluorescence spectra were measured using a Hitachi F-4700 fluorescence spectrophotometer.

2.2. In Vitro Fluorescence Response Assay

Fluorescence spectra were measured using a Hitachi F-4700 fluorescence spectrophotometer. For NO detection, the excitation wavelength (λ_{ex}) was set at 620 nm, and the emission scanning range was configured from 660 to 800 nm. For $O_2^{\bullet-}$ detection, the excitation wavelength (λ_{ex}) was set at 450 nm, with the emission scanning range adjusted to 500–700 nm. The selectivity data were calculated by the formula F/F_0, where F represents the fluorescence intensity of the tested sample and F_0 denotes the fluorescence intensity of the blank sample. All measurements were performed in at least three independent replicates, and the results are presented as mean ± standard deviation (SD) (n = 3).

2.3. Cellular Fluorescence Imaging

Cellular fluorescence imaging was acquired on a Leica confocal microscope (Leica-STELLARIS 5, Wetzlar, Germany). Prior to all imaging operations, the cells were rinsed three times with PBS, and fluorescence imaging was performed under the microscope equipped with a 20× objective lens. For the immunofluorescence assay, after incubation with 60 μg/mL ox-LDL for 48 h, the cells were fixed with 4% paraformaldehyde fixative, permeabilized with Triton X-100 permeabilization solution, and blocked with immunofluorescence blocking buffer. The corresponding primary antibodies against CD36 and CD68 were added, respectively, and the cells were incubated at 4 °C overnight. Subsequently, the cells were incubated with FITC-conjugated and Cy3-conjugated secondary antibody dilutions at room temperature for 2 h. After adding DAPI-containing anti-fade mounting medium, the cells were incubated at room temperature for 10 min, and fluorescence imaging was carried out on the confocal laser scanning microscope. All imaging experiments were repeated three times independently, and the quantitative results are presented as mean ± standard deviation (SD) (n = 3).

2.4. Synthesis of Probe MB-ROS

Under a nitrogen atmosphere, compound 4 (0.39 g, 1 mM), compound 5 (0.35 g, 1 mM) and anhydrous sodium carbonate (0.42 g, 4 mM) were dissolved in 15 mL of anhydrous N,N-dimethylformamide (DMF). The reaction mixture was stirred at 35 °C for 6 h. After the reaction was completed, the insoluble precipitate was removed by filtration. The resulting filtrate was extracted with ethyl acetate and deionized water, and the organic solvent was subsequently removed via rotary evaporation. The crude product was purified by TLC (DCM:CH_3OH = 50:1, v/v). HRMS (ESI): calculated for $C_{32}H_{28}F_3N_5O_6S_2$ $[M + Na]^+$ m/z 722.1331, found m/z 722.1304. ^{1}H NMR (400 MHz, Chloroform-d) δ 8.69 (d, J = 7.1 Hz, 1H), 8.62 (d, J = 8.2 Hz, 1H), 8.41 (d, J = 8.4 Hz, 1H), 7.95–7.90 (m, 1H), 7.73 (d, J = 8.1 Hz, 1H), 7.13 (d, J = 8.8 Hz, 2H), 6.61 (s, 2H), 6.52 (d, J = 8.2 Hz, 2H), 5.34 (t, J = 5.5 Hz, 1H), 4.36 (t, J = 5.6 Hz, 2H), 3.65 (q, J = 5.6 Hz, 2H), 2.89 (s, 12H). ^{13}C NMR (101 MHz, $CDCl_3$) δ 162.69, 162.01, 155.09, 148.15, 147.81, 133.06, 131.52, 130.36, 128.60, 127.63, 127.31, 126.14, 125.91, 123.78, 122.01, 121.73, 119.27, 117.90, 116.08, 110.28, 109.85, 39.69, 39.08, and 38.38.

3. Results and Discussion

In this study, a fluorescent probe, MB-ROS, was designed and synthesized for the simultaneous detection of the changes in $O_2^{\bullet-}$ and NO levels in the macrophage foaming

model (Figure 1a). The detailed synthetic route is illustrated in Figure S1. All key intermediates and the final target product have been systematically characterized and confirmed via ^{1}H Nuclear Magnetic Resonance (^{1}H NMR), ^{13}C Nuclear Magnetic Resonance (^{13}C NMR) and High-Resolution Mass Spectrometry (HRMS) (Figures S2–S9). MB-ROS consists of three functional moieties, where methylene blue serves as the fluorophore for NO detection and 1,8-naphthalimide acts as the recognition fluorophore for $O_2^{\bullet-}$. The two independent fluorophores are covalently connected through a urea linkage, enabling the simultaneous and separate detection of $O_2^{\bullet-}$ and NO, respectively.

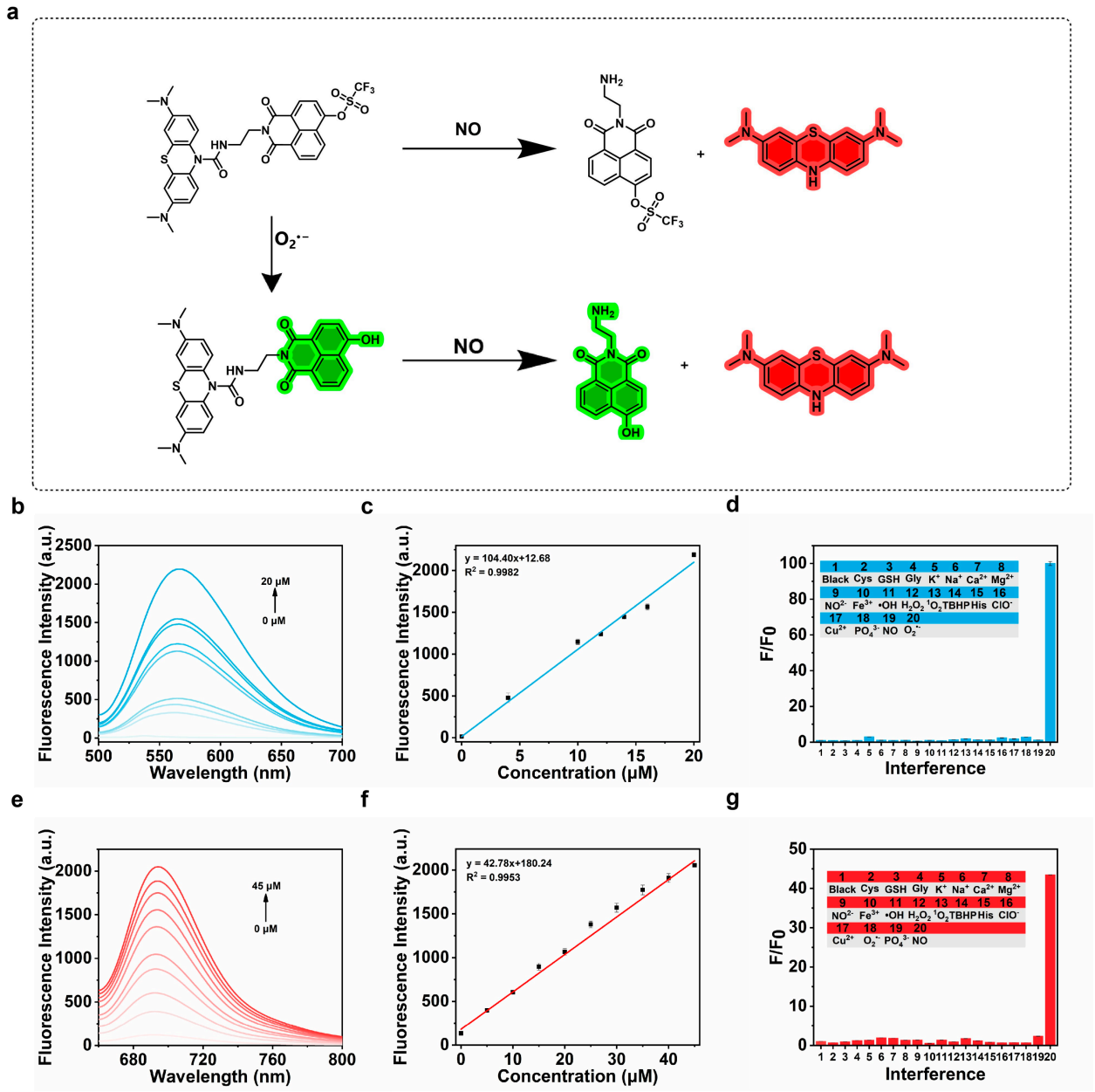

Figure 1. Photophysical properties of the as-synthesized MB-ROS probe. (**a**) Schematic illustration of the chemical structure and response mechanism of MB-ROS. (**b**) Fluorescence response of the probe towards gradient concentrations of $O_2^{\bullet-}$. (**c**) The linear correlation between $O_2^{\bullet-}$ concentration and the fluorescence intensity of MB-ROS at 565 nm. (**d**) The selectivity of the probe for $O_2^{\bullet-}$ detection at the emission wavelength of 565 nm. (**e**) Fluorescence response of the probe towards gradient concentrations of NO. (**f**) The linear correlation between NO concentration and the fluorescence intensity of MB-ROS at 695 nm. (**g**) The selectivity of the probe for NO detection at the emission wavelength of 695 nm.

In this work, the photophysical properties of the probe MB-ROS were systematically investigated at first. Under simulated physiological conditions, the in vitro fluorescence response performance of MB-ROS was comprehensively tested. After adding MB-ROS at a final concentration of 10 μM into PBS buffer solution, $O_2^{\bullet-}$ solution with gradient concentrations ranging from 0 to 20 μM was introduced sequentially. The fluorescence emission of MB-ROS at 565 nm exhibited a concentration-dependent gradual enhancement, with the maximum fluorescence enhancement amplitude reaching up to 100-fold (Figure 1b). Subsequently, the detection capability of MB-ROS towards NO was evaluated under identical experimental conditions. After the addition of NO solution with gradient concentrations from 0 to 45 μM, the fluorescence signal of MB-ROS at 695 nm increased progressively in a dose-dependent manner, achieving a maximum enhancement of 43-fold (Figure 1e). In addition, to verify the independent detection of the two channels of MB-ROS for $O_2^{\bullet-}$ and NO, we verified the detection capability of MB-ROS for $O_2^{\bullet-}$ and NO via a two-dimensional calibration matrix and sequential experiments (Figures S10 and S11). These preliminary results demonstrate that the as-prepared probe possesses detection performance towards both $O_2^{\bullet-}$ and NO in vitro.

Further quantitative investigation verified that MB-ROS exhibits favorable linear fluorescence responses for the detection of $O_2^{\bullet-}$ and NO simultaneously. The fluorescence intensity of MB-ROS at 565 nm showed a well-defined linear increasing trend with the elevation of $O_2^{\bullet-}$ concentration. The corresponding linear regression equation was fitted as $F_{565\ nm} = 104.40\ [O_2^{\bullet-}] + 12.68$, with a linear correlation coefficient of 0.9982, and the limit of detection (LOD) was calculated to be 67 nM (Figure 1c). Meanwhile, the fluorescence intensity at 695 nm presented a positive linear correlation with the increasing NO concentration, with the linear equation determined as $F_{695\ nm} = 42.78\ [NO] + 180.24$, a linear correlation coefficient of 0.9953, and a corresponding limit of detection of 66 nM (Figure 1f). These results collectively confirm that MB-ROS possesses extremely high sensitivity towards both $O_2^{\bullet-}$ and NO.

To systematically evaluate the detection specificity of MB-ROS towards $O_2^{\bullet-}$ and NO in complex biological matrices ranging from living cells to in vivo systems, the anti-interference performance of the probe was characterized under simulated physiological conditions. A series of coexisting components, including various amino acids, biologically relevant metal ions, and other reactive oxygen species and reactive nitrogen species, were separately introduced into PBS solutions containing MB-ROS. After the addition of these interfering substances, fluorescence signal variations at 565 nm and 695 nm could only be triggered by the presence of $O_2^{\bullet-}$ and NO, respectively, while all other tested components induced negligible changes to the intrinsic fluorescence of the probe (Figure 1d,g). The results demonstrate that MB-ROS possesses the capability for selective detection of $O_2^{\bullet-}$ and NO. Furthermore, the probe exhibits operational stability for $O_2^{\bullet-}$ and NO detection under physiological conditions, with its fluorescence intensity remaining nearly unchanged over a continuous monitoring period of 1800 s (Figure S12). All these in vitro characterization results collectively confirm the reliable sensing performance of MB-ROS for the two target analytes.

In view of the in vitro detection performance of MB-ROS for $O_2^{\bullet-}$ and NO, the cytotoxicity profile of the probe was comprehensively assessed via CCK-8 assay prior to cellular imaging experiments to guarantee the validity and reliability of subsequent fluorescence imaging tests. RAW 264.7 macrophages were incubated with MB-ROS at gradient concentrations spanning 0 to 80 μM. After 24 h of incubation, the cell viability remained higher than 80% (Figure S13). This result demonstrates that the MB-ROS probe possesses biocompatibility.

To further verify that the MB-ROS probe can detect $O_2^{\bullet-}$ and NO at the cellular level, confocal fluorescence imaging was performed on RAW 264.7 cells. 2-ME can elevate intracellular $O_2^{\bullet-}$ levels by inhibiting the activity of superoxide dismutase (SOD) [27]. After incubating RAW 264.7 cells with 3 μg/mL 2-ME, the fluorescence intensity in the green channel increased by approximately 3.56-fold compared with the control group (Figure 2a,c). These results demonstrate that MB-ROS is capable of detecting the variation in $O_2^{\bullet-}$ at the cellular level. Subsequently, to validate the capability of the probe for monitoring NO changes in living cells, confocal fluorescence imaging of RAW 264.7 cells was carried out. After stimulation with 50 μM NO, the fluorescence intensity in the red channel increased by approximately 3.29-fold (Figure 2b,d). To further verify the selective NO detection performance of the probe at the cellular level, Carboxy-PTIO, a specific NO scavenger, was employed to eliminate intracellular NO [28]. After Carboxy-PTIO treatment, the fluorescence intensity in the red channel decreased by approximately 5.28-fold compared with the NO-stimulated group. These results demonstrate that the MB-ROS probe can effectively detect the fluctuation of NO at the cellular level (Figure 2b,d).

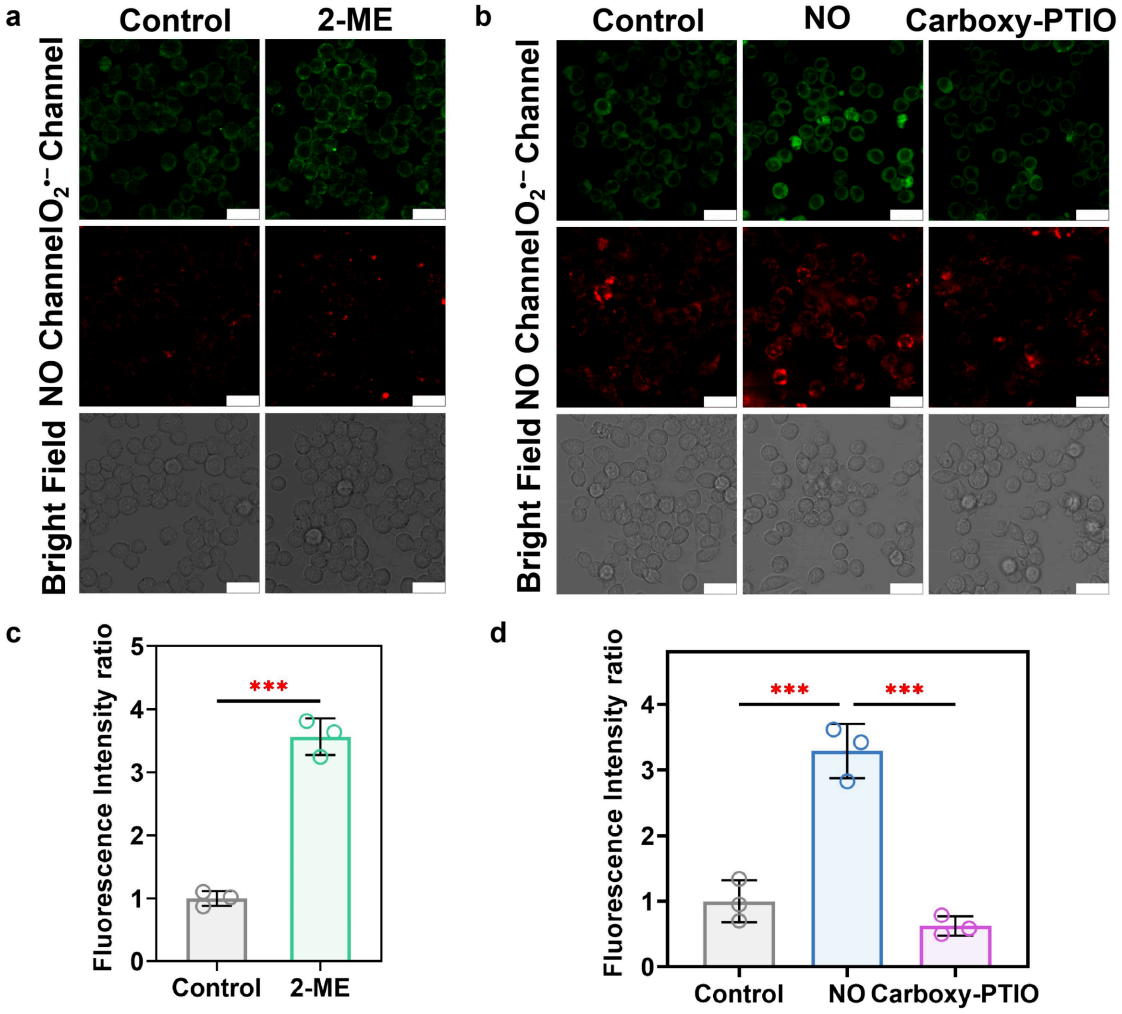

Figure 2. Fluorescence imaging experiments at the cellular level. (**a**) Confocal fluorescence imaging of MB-ROS for detecting endogenous $O_2^{\bullet-}$ in RAW 264.7 macrophages under 2-ME stimulation. (**b**) Confocal fluorescence imaging of MB-ROS for detecting NO in RAW 264.7 macrophages under exogenous NO stimulation. (**c**) Fluorescence intensity output of the $O_2^{\bullet-}$ channel in panel (**a**). (**d**) Fluorescence intensity output of the NO channel in panel (**b**). Scale bar = 20 μm.

To validate the successful establishment of the macrophage foam cell model, the intracellular ROS level in the foam cell model was detected using the DCFH-DA probe, and the expression changes in CD68 and CD36 were characterized via immunofluorescence staining [29,30]. After incubation with 60 μg/mL ox-LDL, the fluorescence intensity of ROS in the foam cell model increased by 4.17-fold compared with the control group (Figure 3a,b). Under the same 60 μg/mL ox-LDL treatment, the expression level of CD68 in the foam cell model was approximately 1.87 times higher than that of the control group, while the expression level of CD36 increased by about 2.1-fold relative to the control (Figure 3c–f). These results confirm that the macrophage foam cell model was successfully constructed.

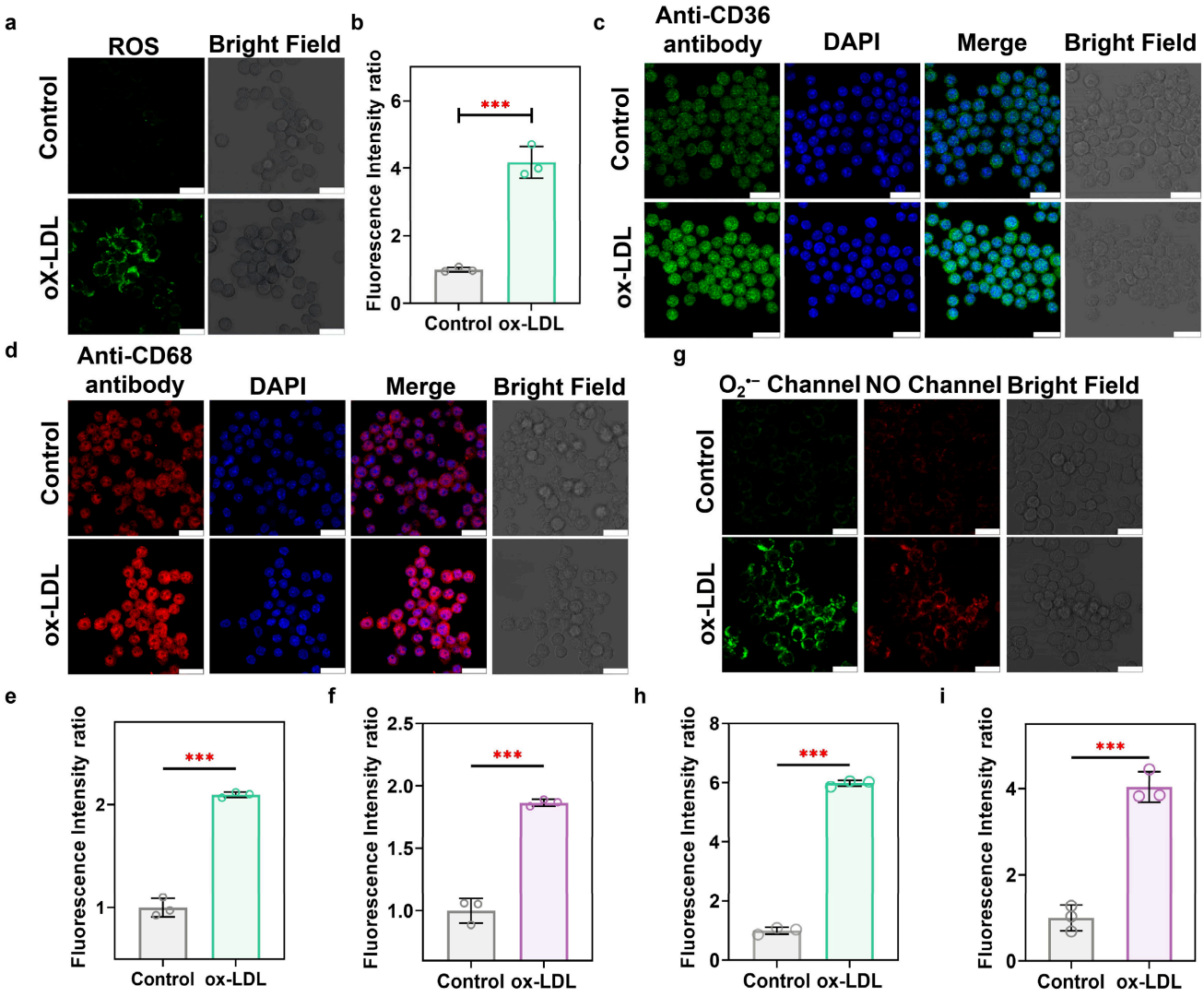

Figure 3. Fluorescence imaging of ox-LDL-induced macrophage-derived foam cells. (**a**) Fluorescence imaging of total ROS in foam cells stained with DCFH-DA probe. (**b**) Quantitative fluorescence intensity analysis corresponding to the imaging groups in panel (**a**). (**c**) Immunofluorescence co-staining imaging of CD36 (lipid scavenger receptor) and DAPI (nuclear marker) in foam cells. (**d**) Immu-nofluorescence co-staining imaging of CD68 (macrophage-specific marker) and DAPI (nuclear marker) in foam cells. (**e**) Quantitative fluorescence intensity analysis corresponding to the imaging groups in panel (**c**). (**f**) Quantitative fluorescence intensity analysis corresponding to the imaging groups in panel (**d**). (**g**) Simultaneous dual-channel fluorescence imaging of the level variations in $O_2^{\bullet-}$ and NO in foam cells labeled with MB-ROS probe. (**h**) Fluorescence intensity output of the $O_2^{\bullet-}$ channel in panel (**g**). (**i**) Fluorescence intensity output of the NO channel in panel (**g**). Scale bar = 20 μm.

Subsequently, to investigate the changes in $O_2^{\bullet-}$ and NO levels during the macrophage foam formation process, RAW 264.7 cells were stimulated with 60 μg/mL ox-LDL for 48 h, and the alterations of intracellular $O_2^{\bullet-}$ and NO levels were detected using the MB-ROS probe. After 48 h of ox-LDL stimulation, the fluorescence intensity in the $O_2^{\bullet-}$ detection channel increased by approximately 5.98-fold, and the fluorescence intensity in the NO detection channel increased by about 4.04-fold, compared with the normal group (Figure 3g–i). These findings demonstrate that MB-ROS is capable of evaluating the variations in $O_2^{\bullet-}$ and NO levels during the progression of macrophage foam cell formation.

4. Conclusions

In this work, a novel dual-response fluorescent probe, MB-ROS, was successfully synthesized for the simultaneous detection of level variations in $O_2^{\bullet-}$ and NO during the macrophage foaming process. Under simulated physiological conditions, MB-ROS exhibits high comprehensive sensing performance towards $O_2^{\bullet-}$ and NO, including high sensitivity, specificity and photostability. In the ox-LDL-induced macrophage foaming model, significant upregulation of both $O_2^{\bullet-}$ and NO levels was clearly visualized with the assistance of MB-ROS. This specific probe provides a critical visualized analytical tool for revealing the alteration of oxidative stress status in the pathological progression of macrophage foaming. Therefore, MB-ROS serves as a reliable chemical imaging platform for in-depth mechanistic investigations of redox imbalance during the macrophage foaming process.

Supplementary Materials: The following supporting information can be downloaded at: https://www.mdpi.com/article/10.3390/targets4030027/s1. Figure S1. Synthetic route of MB-ROS; Figure S2. The High-Resolution Mass Spectrum of Compound 1; Figure S3. The High-Resolution Mass Spectrum of Compound 2; Figure S4. The High-Resolution Mass Spectrum of Compound 3; Figure S5. The High-Resolution Mass Spectrum of Compound 4; Figure S6. The High-Resolution Mass Spectrum of Compound 5; Figure S7. The High-Resolution Mass Spectrum of Compound 6; Figure S8. ^{1}H NMR spectrum of MB-ROS; Figure S9. ^{13}C NMR spectrum of MB-ROS; Figure S10. Two-dimensional calibration matrix of MB-ROS; Figure S11. Fluorescence response spectra of MB-ROS after sequential addition of $O_2^{\bullet-}$ followed by NO. (a) Fluorescence response spectrum of MB-ROS toward $O_2^{\bullet-}$. (b) Fluorescence response spectrum of MB-ROS toward NO; Figure S12. Time-dependent fluorescence intensity changes of MB-ROS. (a) Timecourse variations of fluorescence intensity of MB-ROS before and after reaction with $O_2^{\bullet-}$. (b) Time-dependent fluorescence intensity changes of MB-ROS before and after reaction with NO; Figure S13. Cell viability of RAW 264.7 cells after incubation with MB-ROS at concentrations ranging from 0 to 50 μM; Table S1. Summary of $O_2^{\bullet-}$-responsive optical probe; Table S2. Summary of NO-responsive optical probe.

Author Contributions: X.C. performed the experiment; X.C., J.L., C.W., W.Z. (Wen Zhang), H.W., W.Z. (Wei Zhang), P.L. and B.T. analyzed the experimental data; X.C., J.L., W.Z. (Wei Zhang) and B.T. wrote the manuscript. All authors have read and agreed to the published version of the manuscript.

Funding: This work was supported by the National Natural Science Foundation of China (22134004 and 22374091).

Institutional Review Board Statement: Not applicable.

Informed Consent Statement: Not applicable.

Data Availability Statement: Data will be made available on request.

Conflicts of Interest: The authors declare no conflicts of interest.

References

1. Engelen, S.E.; Robinson, A.J.B.; Zurke, Y.-X.; Monaco, C. Therapeutic strategies targeting inflammation and immunity in atherosclerosis: How to proceed? *Nat. Rev. Cardiol.* **2022**, *19*, 522–542. [CrossRef] [PubMed]
2. Gisterå, A.; Hansson, G.K. The immunology of atherosclerosis. *Nat. Rev. Nephrol.* **2017**, *13*, 368–380. [CrossRef] [PubMed]
3. Lu, Y.; Shi, B.; Chen, J.; Yao, H.; Mi, X.; Shao, M.; Zhao, Y.; Meng, L.; Tai, Q.; Chen, J.; et al. Insights into macrophage ferroptosis: Implications for atherosclerosis. *Cell Prolif.* **2026**, *59*, e70154.
4. Zhi, X.; Sun, Y.; Cai, F.; Wang, S.; Gao, H.; Wu, F.; Zhang, L.; Shen, Z. Oxidized low-density lipoprotein (Ox-LDL)-triggered double-lock probe for spatiotemporal lipoprotein oxidation and atherosclerotic plaque imaging. *Adv. Healthc. Mater.* **2023**, *12*, 2301595. [CrossRef] [PubMed]
5. Ding, J.; Li, H.; Liu, W.; Wang, X.; Feng, Y.; Guan, H.; Chen, Z. miR-186-5p dysregulation in serum exosomes from patients with AMI aggravates atherosclerosis via targeting LOX-1. *Int. J. Nanomed.* **2022**, *17*, 6301–6316. [CrossRef] [PubMed]
6. Yang, X.; Shang, D. The role of peroxisome proliferator-activated receptor γ in lipid metabolism and inflammation in atherosclerosis. *Cell Biol. Int.* **2023**, *47*, 1469–1487. [CrossRef] [PubMed]
7. Kwon, N.; Kim, D.; Swamy, K.M.K.; Yoon, J. Metal-coordinated fluorescent and luminescent probes for reactive oxygen species (ROS) and reactive nitrogen species (RNS). *Coord. Chem. Rev.* **2021**, *427*, 213581. [CrossRef]
8. Zhou, L.; Wang, Z.; Wang, L.; Zhang, X.; Xiao, Y. Tetrazine-based ratiometric nitric oxide sensor identifies endogenous nitric oxide in atherosclerosis plaques by riding macrophages as a smart vehicle. *J. Am. Chem. Soc.* **2023**, *145*, 28296–28306. [CrossRef] [PubMed]
9. Ye, Z.; Ji, M.; Wu, K.; Yang, J.; Liu, A.; Sun, W.; Ding, D.; Liu, D. In-sequence high-specificity dual-reporter unlocking of fluorescent probe enables the precise identification of atherosclerotic plaques. *Angew. Chem. Int. Ed.* **2022**, *61*, e202204518. [CrossRef] [PubMed]
10. Peng, T.; Wong, N.-K.; Chen, X.; Chan, Y.-K.; Sun, Z.; Hu, J.J.; Shen, J.; El-Nezami, H.; Yang, D. Molecular imaging of peroxynitrite with HKGreen-4 in live cells and tissues. *J. Am. Chem. Soc.* **2018**, *140*, 854. [CrossRef] [PubMed]
11. Wang, C.; He, Y.; Tang, J.; Mao, J.; Liang, X.; Xu, M.; Zhang, Z.; Tian, J.; Jiang, J.; Li, C.; et al. Chondroitin sulfate functionalized nanozymes inhibit the inflammation feedback loop for enhanced atherosclerosis therapy by regulating intercellular crosstalk. *Int. J. Biol. Macromol.* **2024**, *282*, 136918. [CrossRef] [PubMed]
12. Li, Y.; Yu, T.; Wang, Z.; Wang, J.; Tang, Y.; Zhang, Y.; Li, H.; Zhou, H.; Yin, P.; Yao, S. A fluorescent probe for concurrent detection of cysteine, homocysteine, and superoxide anion. *Sci. Adv.* **2025**, *11*, eadx6659. [CrossRef] [PubMed]
13. Ma, Y.; Cao, H.; Chen, B.; Xu, X.; Zhang, Q.; Chen, H.; Zhang, X.; Song, G. Simultaneous in vivo imaging of neutrophil elastase and oxidative stress in atherosclerotic plaques using a unimolecular photoacoustic probe. *Angew. Chem. Int. Ed.* **2024**, *63*, e202411840. [CrossRef] [PubMed]
14. Ma, Y.; Xu, L.; Yin, B.; Shang, J.; Chen, F.; Xu, J.; Song, Z.; Nan, B.; Song, G.; Zhang, X. Ratiometric semiconducting polymer nanoparticle for reliable photoacoustic imaging of pneumonia-induced vulnerable atherosclerotic plaque in vivo. *Nano Lett.* **2021**, *21*, 4484–4493. [CrossRef] [PubMed]
15. Tousoulis, D.; Kampoli, A.; Papageorgiou, C.T.N.; Stefanadis, C. The role of nitric oxide on endothelial function. *Curr. Vasc. Pharmacol.* **2012**, *10*, 4–8. [CrossRef] [PubMed]
16. Giesen, J.; Menges, L.; Benndorf, R.A. Tissue-specific regulation of NO-GC isoforms in the cardiovascular system. *Biochem. Pharmacol.* **2025**, *242*, 117384. [CrossRef] [PubMed]
17. Kaesemeyer, W.H.; Caldwell, R.W. Atherosclerosis and nitric oxide production. *Circulation* **2000**, *102*, e90. [CrossRef] [PubMed]
18. Wang, B.; Hoai-Ky, V.H.; Patrick, S.L.; Severin, P.S.; Matthew, J.P.; Gary, H.G.; Philip, S.T.; John, P.C. Regression of atherosclerosis: Role of nitric oxide and apoptosis. *Circulation* **1999**, *99*, 1236–1241. [PubMed]
19. Xu, W.; Chen, D.; Zhou, H.L. S-nitrosylation: Mechanistic links between nitric oxide signaling and atherosclerosis. *Curr. Atheroscler. Rep.* **2025**, *27*, 78. [CrossRef] [PubMed]
20. Volodymyr, I.L.; Oleh, L. Interplay between reactive oxygen and nitrogen species in living organisms. *Chem. Biol. Interact.* **2021**, *349*, 109680. [CrossRef] [PubMed]
21. Cao, H.; Meng, X.; Ma, Y.; Li, Z.; Xu, X.; Fu, J.; Zhang, Q.; Wei, H.; Liang, P.; Lu, D.; et al. Neutrophil elastase-activatable ratiometric photoacoustic nanoprobes for imaging atherosclerotic plaque vulnerability. *Nat. Commun.* **2025**, *16*, 9635. [CrossRef] [PubMed]
22. Li, J.; Miao, Y.; Pan, W.; Li, N.; Tang, B. Thiol-polarity dual cascade–triggered two-photon imaging of protein unfolding for early atherosclerosis diagnosis. *Sci. Adv.* **2025**, *11*, eaea3727. [CrossRef] [PubMed]
23. Huang, X.; Si, W.; Li, G.; Zhou, Y.; Tang, Y.; Gao, W.; Tang, B. Lighting up ferroptosis propagating via the lung-heart axis exacerbates cardiovascular disease through in situ imaging. *Angew. Chem. Int. Ed.* **2026**, *65*, e7388558. [CrossRef] [PubMed]
24. Wei, F.; Ding, Y.; Ou, J.; Chen, X.; Li, L.; Zhou, Q.; Chen, Q.; Wang, Q.; Feng, Y.; Meng, X. Accurate detection of Hcy in human serum and two-photon visualization of atherosclerosis using a highly specific fluorescent probe. *Anal. Chem.* **2023**, *95*, 9173–9181. [CrossRef] [PubMed]

25. Ji, M.; Wei, Y.; Ye, Z.; Hong, X.; Yu, X.; Du, R.; Li, Q.; Sun, W.; Liu, D. In vivo fluorescent labeling of foam cell-derived extracellular vesicles as circulating biomarkers for in vitro detection of atherosclerosis. *J. Am. Chem. Soc.* **2024**, *146*, 10093–10102. [CrossRef] [PubMed]
26. Ma, Y.; Wang, K.; Yang, F.; Wei, H.; Li, C.; Mao, H.; Ying, J.; Yu, J.; Ying, S.; Shen, J.; et al. A tandem-responsive probe for dual-enzyme photoacoustic imaging of atherosclerotic plaque in vivo. *Anal. Chem.* **2025**, *97*, 22359–22367. [CrossRef] [PubMed]
27. Liu, J.; Zhang, W.; Wang, X.; Ding, Q.; Wu, C.; Zhang, W.; Wu, L.; James, T.D.; Li, P.; Tang, B. Unveiling the crucial roles of $O_2^{\bullet-}$ and ATP in hepatic ischemia–reperfusion injury using dual-color/reversible fluorescence imaging. *J. Am. Chem. Soc.* **2023**, *145*, 19662–19675. [CrossRef] [PubMed]
28. Xiao, F.; Jiang, H.; Li, Z.; Jiang, X.; Chen, S.; Niu, Y.; Yin, H.; Shu, Y.; Peng, B.; Lu, W.; et al. Reduced hepatic bradykinin degradation accounts for cold-induced BAT thermogenesis and WAT browning in male mice. *Nat. Commun.* **2023**, *14*, 2523. [CrossRef] [PubMed]
29. Chen, S.; Zhang, W.; Tang, C.; Rong, X.; Liu, Y.; Luo, Y.; Xu, L.; Xu, Z.; Wang, J.; Wang, Y.; et al. Macrophage membrane-functionalized manganese dioxide nanomedicine for synergistic treatment of atherosclerosis by mitigating inflammatory storms and promoting cholesterol efflux. *J. Nanobiotechnol.* **2024**, *22*, 664. [CrossRef] [PubMed]
30. Moore, K.J.; Sheedy, F.J.; Fisher, E.A. Macrophages in atherosclerosis: A dynamic balance. *Nat. Rev. Immunol.* **2013**, *13*, 709–721. [CrossRef] [PubMed]